## DSCC2018-9211

# EDDY-CURRENT DYNAMIC MODEL FOR SIMULTANEOUS GEOMETRICAL AND MATERIAL PARAMETER MEASUREMENTS OF MAGNETIC MATERIALS

Bingjie Hao<sup>1, 2</sup> Kok-Meng Lee<sup>1, 2, \*</sup> Kun Bai<sup>1, \*</sup>

- <sup>1</sup> State Key Lab. of Dig. Manuf. Equip. and Tech., Huazhong Univ. of Sci. and Tech., Wuhan, Hubei, China
- <sup>2</sup> George W. Woodruff Sch. of Mech. Eng., Georgia Inst. of Tech., Atlanta, GA 30332, USA
- \* Corresponding Authors' Emails: kokmeng.lee@me.gatech.edu; kbai@hust.edu.cn

## **ABSTRACT**

This paper presents a distributed current source (DCS) method for modeling the dynamic responses of eddy current density (ECD) induced in electrical conductors and its corresponding magnetic flux density (MFD); both nonmagnetic and weakly magnetized conductors are considered. Unlike conventional numerical methods such as finite element analysis (FEA), the DCS method, which accounts for the eddy-current and magnetization effects by means of equivalent volume and surface current-sources, derives closed-form solutions to the ECD and MFD fields in state-space representation. model has been experimentally validated and verified by comparing results from FEA simulations with both harmonic and nonharmonic excitations. To gain physical insights to the measured **MFD** for simultaneous estimating material/geometrical properties of a conductor, the static and dynamic responses to rectangular pulsed current excitations have been numerically investigated, confirming the feasibility and effectiveness of the measurement methods.

#### **NOMENCLATURE**

## Lowercase symbols

a, a<sub>i</sub>, a<sub>o</sub>
 h, w
 Half-height, inner and outer radii of EM thickness and radius of conductor
 MFD sensor to conductor distance

 $\mathbf{r}_s \ (r_s, -z_s)$  Location and cylindrical coordinates of MFD sensor  $\hat{v}, \hat{s}$  Cross-section area of volume, length of surface element

Input/excitation current

Uppercase symbols

A Magnetic vector potential (MVP)
B Magnetic flux density (MFD)
H Magnetic field intensity
M Magnetization vector
J Eddy current density (ECD)

 $J_m$ , K Equivalent magnetized volume and surface current density

A, J, K Circumferential ( $\theta$ ) components of A, J, K

Greek symbols

 $\mu_0, \mu_r$  Vacuum permeability and relative permeability

 $\chi_m$  Magnetic susceptibility  $\sigma$  Electrical conductivity  $\omega$  Angular frequency in rad/s

#### INTRODUCTION

Eddy current (EC) sensors have a broad spectrum of applications ranging from sensing of geometry and material parameters [1, 2], to eddy-current-based actuating/damping devices [3], to induction heating [4], and more recently biomedical applications [5]. Among these, EC is the most commonly found medium in high-precision non-contact measurements due to its good penetrability and workability in harsh environment. It provides an excellent means in industrial applications for displacement and thickness measurements, conductivity estimation, and defect detection.

Many EC-based systems or devices assume the material to be conductive but non-magnetic metals, in which case the magnetization effects are neglected. As a dynamic system, the ECD distribution in a non-magnetic conductor is determined by measuring the variation in the MFD field generated by both the input excitation and self/mutual induction. EC also influences the physical magnetic field, force and heat distribution.

The EC models that describe the frequency response under harmonic excitation have been widely studied in applications to analyze EC-based sensor designs. Dodd et al. proposed a wellknown analytical model [6] which was later improved by Theodoros et al. [7] to achieve fast solving through a truncated region eigenfunction expansion method. Besides, transformer models were widely utilized to simplify the analytical methods [8]. However, many applications require transient response analyses of the ECD under more complicated excitation. For examples, the pulsed-EC technology has replaced the sinusoidal excitation in eddy current sensing to improve penetration in conductor and acquire more physical information [2] [9]. In parallel to these developments, the heat generated by pulsed-EC can be captured by a thermal imager to detect multiple cracks [10]. In actuation applications, transient EC forces can be used in electrodynamic magnetic levitation [11]. To handle these problems, a state-space modeling method was proposed in [12] to analyze the EC response.

Metals like carbon steel and stainless steel (such as EOS

PH1) that have relatively low permeability are commonly employed in manufacturing applications including machining and additive manufacturing (AM) due to their excellent mechanical properties. Improper geometrical dimension and material properties may exist during the AM process [13]; for example, the potential phase transform (from austenite to martensite) of stainless steel that is highly related to the magnetic permeability could affect the final mechanical property [14]. Eddy currents which have been widely studied for non-magnetic conductors have the potentials for sensing magnetic materials in monitoring AM processes. However, EC sensing involving magnetic conductors are complicated because the magnetization effects in the conductor, which generate additional MFDs, further influence the ECD distribution. To account for the magnetization effects, assumptions commonly made in analytically derived solutions must be relaxed.

Originally proposed in [12][15], the distributed current source (DCS) method presents a generalized source modeling method to characterize commonly used magnetic components for analyzing electromagnetic actuators. The DCS method can account for edge effects and proximity effects among adjacent elements, which are commonly neglected in analytically derived solutions. As compared with FEA methods which require a sufficiently large air space to enclose all the magnetic fields that generated by EM, EC and magnetization to ensure accuracy, the DCS method requires only to mesh the conductor, eliminating the need to model the air space. Inspired by the DCS method [12] which offers closed-form solutions to the EC field in non-magnetic conductors, this paper extends the previous work to account for the magnetization effects of the magnetic materials. The remainder of this paper offers the following:

- The DCS model, which accounts for the magnetization effects of the material due to an external time-varying magnetic field, is introduced. For clarity in illustration, the 2D axisymmetric EC and equivalent surface current are formulated in state-space representation; both harmonic excitation and non-harmonic excitations are considered.
- 2) The DCS model has been experimentally validated using a nonmagnetic and a weakly magnetized samples. The effects of the magnetic permeability on the measured MFDs are examined by comparing results simulated with and without magnetic properties.
- A numerical investigation has been conducted to verify the model accuracy by comparing the DCS-based solutions with FEA solutions; both harmonic excitation and nonharmonic excitations are considered.
- 4) The effectiveness of the DCS models is numerically demonstrated for simultaneous EC-based measurements of the geometrical (distance and thickness) and material (permeability and conductivity) properties.

## **DISTRIBUTED-PARAMETER EDDY-CURRENT MODEL**

Figure 1 schematically models a typical EC-based sensing

system where an excitation electromagnet (EM) generates an arbitrary time-varying magnetic flux density (MFD) and thus induces EC field in the conductor (with electrical conductivity  $\sigma$  and relative magnetic permeability  $\mu_r$ ). The parametric effect of the conductor (geometrical and/or material property) on the EC field is measured by a MFD sensor located at  $(r_s, -z_s)$  in the cylindrical coordinate system assigned at the EM center. Since the MFD field due to the applied current u(t) following through the EM is known and can be subtracted from the measurement, the derivation here focuses the effects of the induction and magnetization of the conductor and their corresponding MFDs generated in the space on measurements. For deriving practical solutions, the conductor is decomposed into n volume elements and m surface elements as shown in Fig. 1, which are modeled as individual volume current density (VCD) sources and surface current density (SCD) sources, and solved using the DCS method.

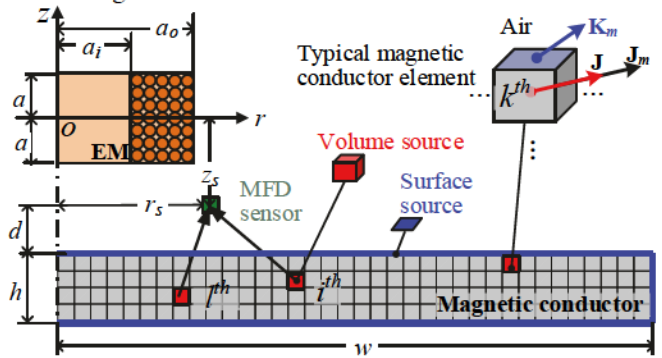


FIGURE 1. SCHEMATICS OF DCS MODEL FOR EM/CONDUCTOR SYSTEM

## Governing equations

The following assumptions are made in developing the state-space field model: 1) The electromagnetic materials are isotropic and homogeneous enabling the macroscopic continuum approximation of the field. 2) The magnetic material is soft or operates within a linear region with negligible hysteresis effects such that the MFD  $\mathbf{B} = \mu_0 \mu_r \mathbf{H}$  where  $\mathbf{H}$  is the magnetic field intensity;  $\mu_0$  is the permeability of free space (air). 3) The electric current in the conductor obeys Ohm's law. 4) The operating frequencies are low  $(f \le 1 \text{MHz})$  satisfying magneto quasi-static conditions.

The magnetization effects of the conductor are due to induction by the ECD (vector  $\mathbf{J}$ ) and magnetization (vector  $\mathbf{M}$ ). The latter is equivalent to a VCD  $\mathbf{J}_m$  and SCD  $\mathbf{K}$  of the forms:

$$\mathbf{J}_{m} = \nabla \times \mathbf{M} \quad \text{and} \quad \mathbf{K} = \mathbf{M} \times \mathbf{n}$$
 (1a, b)

where **n** is the normal vector out of the conductor surface. Using the Maxwell equation  $(\mathbf{J} = \nabla \times \mathbf{H})$  and the constitutive equation  $(\mathbf{M} = \chi_m \mathbf{H})$  where  $\chi_m (= \mu_r - 1)$  is the magnetic susceptibility,  $\mathbf{J}_m$  due to the magnetization  $\mathbf{M}$  in the conductor can be expressed as

$$\mathbf{J}_{m} = \nabla \times (\chi_{m} \mathbf{H}) = \chi_{m} \mathbf{J} \tag{2a}$$

Then the total volume current density in the conductor is

$$\mathbf{J} + \mathbf{J}_m = \mu_r \mathbf{J} \tag{3}$$

To account for the boundary effect of the magnetic material on the measured MFD, a conceptual SCD **K** [15] due to the MFD **B** is introduced for the k<sup>th</sup> surface element:

$$\mathbf{K}_{k} = \gamma \left( \mathbf{B}_{k} \cdot \mathbf{t}_{k} \right) \left( \mathbf{t}_{k} \times \mathbf{n}_{k} \right) \text{ where } \gamma = \frac{2}{\mu_{0}} \frac{\mu_{r} - 1}{\mu_{r} + 1}$$
 (4a, b)

In (4),  $\mathbf{t}$  and  $\mathbf{n}$  are the unit tangential and normal vectors of the  $k^{th}$  element surface.

The induced ECD can be explicitly expressed in terms of geometry-dependent magnetic vector potential (MVPs)  $\mathbf{A}(=\mathbf{A}_e + \mathbf{A}_v + \mathbf{A}_b)$  where  $\mathbf{A}_e$  and  $(\mathbf{A}_v, \mathbf{A}_b)$  are contributed by the timevarying magnetic fields of the EM and of the (VCD, SCD) sources of the conductor respectively. For a DCS model that contains n VCD sources (each with elemental volume v) and m SCD sources (each with elemental surface area s), the ECD in the  $i^{\text{th}}$  volume element can be expressed as

$$\mathbf{J}_{i} = -\sigma \frac{\partial}{\partial t} \left( \mathbf{A}_{ei} + \sum_{k=1}^{n} \mathbf{A}_{vik} + \sum_{l=1}^{m} \mathbf{A}_{bil} \right)$$
 (5)

Similarly,  $\mathbf{B}_k$  (= $\mathbf{B}_e$ +  $\mathbf{B}_v$ +  $\mathbf{B}_b$ ) for computing the surface current density in (4) can be expressed as

$$\mathbf{B}_{k} = \mathbf{B}_{ek} + \sum_{l=1}^{n} \mathbf{B}_{vkl} + \sum_{i=1}^{m} \mathbf{B}_{bki}$$
 (6)

For clarity, the components in the right sides of (5) and (6) are derived for an axisymmetric system reducing to a 2D (r, z) problem. 3D problems, though tedious, can be solved similarly.

## 2D Axisymmetric state-space eddy-current model

For an axisymmetric system,  $(\mathbf{A}_i, \mathbf{J}_i, \mathbf{K}_i)$  have zero r and z components thus are reduced to scalar  $(A_{\theta i}, J_{\theta i}, K_{\theta i})$ . For simplicity, the subscript " $\theta$ " is dropped in the 2D axisymmetric formulation. In contrast,  $\mathbf{B}_k$  has two components;

$$\mathbf{B}_k = \begin{bmatrix} B_{rk} & B_{zk} \end{bmatrix}^{\mathrm{T}}.$$

MVP and MFD contributed by EM

Since the EM geometry is known, the  $1^{st}$  term in the parenthesis on the left side of (5) can be derived from the integral in (7a) where  $C_0$  is the current density with unit current (1 Ampere) flowing through the EM:

$$\frac{A_{ei}}{u} = f_i^e(r_i, z_i) = \frac{\mu_0 C_0}{4\pi} \int_0^{2\pi} \int_{-a_0}^{a_0} \frac{\cos \theta}{|\mathbf{r}_i - \mathbf{r}|} r dr dz d\theta$$
 (7a)

where  $\mathbf{r}_i = \begin{bmatrix} r_i \cos \theta_i & 0 & z_i \end{bmatrix}^T$ ;  $\mathbf{r} = \begin{bmatrix} r \cos \theta & r \sin \theta & z \end{bmatrix}^T$ ; and the superscript "e" denotes the EM. The position vectors,  $\mathbf{r}_i$  and  $\mathbf{r}$ , characterize a point in the conductor being evaluated and a source point in the EM, respectively. Using the Biot-Savart law,  $\mathbf{B}_e$  generated by the EM for computing the SCD in (4) can be found similarly:

$$\frac{\mathbf{B}_{ek}}{u} = \mathbf{g}_{k}^{e}(r_{k}, z_{k}) = \left[ \left( g_{k}^{e} \right)_{r} \quad \left( g_{k}^{e} \right)_{z} \right]^{\mathrm{T}} \\
= \frac{\mu_{0} C_{0}}{4\pi} \int_{0}^{2\pi} \int_{-a}^{a} \int_{a_{k}}^{a_{k}} \left[ r - r_{k} \cos \theta \right] \frac{r dr dz d\theta}{\left| \mathbf{r}_{k} - \mathbf{r} \right|^{3}}$$
(7b)

MVP and MFD contributed by the magnetic conductor

The MVPs  $(A_v, A_b)$  account for the mutual induction among the conductor elements and boundary effect of the magnetic material and are defined in (8a, b) respectively, where  $\hat{v}_l$  and  $\hat{s}_k$  are the corresponding cross-sectional area of  $l^{\text{th}}$  volume element and length of the  $k^{\text{th}}$  surface element:

$$\frac{A_{il}^{v}}{J_{l}\mu_{r}\hat{v}_{l}} = f_{il}^{v}\left(\mathbf{r}_{i}, \mathbf{r}_{l}\right) \text{ and } \frac{A_{ik}^{b}}{K_{k}\hat{s}_{k}} = f_{ik}^{b}\left(\mathbf{r}_{i}, \mathbf{r}_{k}\right)$$
(8a,b)

The kernel function  $f_{nm}^*$  in (8a, b) calculates the MVP at  $\mathbf{r}_n$  by a unit current loop located at  $\mathbf{r}_m$ :

$$f_{nm}^{*}(\mathbf{r}_{n}, \mathbf{r}_{m}) = \frac{\mu_{0}}{4\pi} \int_{0}^{2\pi} \frac{r_{m} \cos \theta d\theta}{\sqrt{(r_{n} - r_{m} \cos \theta)^{2} + (r_{m} \sin \theta)^{2} + (z_{n} - z_{m})^{2}}}$$
(8c)

Similarly,  $(\mathbf{B}_{\nu}, \mathbf{B}_{b})$  for computing the SCD are given in (9a, b) where the kernel function  $\mathbf{g}_{k_{0}}^{*}$  is defined in (9c):

$$\frac{\mathbf{B}_{kl}^{v}}{J_{l}\mu_{r}\hat{v}_{l}} = \mathbf{g}_{kl}^{v}\left(\mathbf{r}_{k}, \mathbf{r}_{l}\right) \text{ and } \frac{\mathbf{B}_{ki}^{b}}{K_{i}\hat{s}_{i}} = \mathbf{g}_{ki}^{b}\left(\mathbf{r}_{k}, \mathbf{r}_{i}\right)$$
(9a,b)

where 
$$\mathbf{g}_{k\circ}^*(\mathbf{r}_k,\mathbf{r}_\circ) = \left[ \left( g_{k\circ}^* \right)_r \quad \left( g_{k\circ}^* \right)_z \right]^{\mathrm{T}} =$$

$$\frac{\mu_0}{4\pi} \int_0^{2\pi} \frac{\left[ \left( r_\circ - r_k \cos \theta \right) \left( z_k - z_\circ \right) \cos \theta \right]^{\mathsf{T}} r dr dz d\theta}{\left[ \left( r_k - r_\circ \cos \theta \right)^2 + \left( r_\circ \sin \theta \right)^2 + \left( z_k - z_\circ \right)^2 \right]^{3/2}}$$
(9c)

State-space representation

Collectively, the VCDs in n volume elements, SCDs in m surface elements and the sensor output  $\mathbf{B}(\mathbf{r}_s)$  can be written in vector forms:

$$\mathbf{J}(\in \mathbb{R}^{n \times 1}) = \begin{bmatrix} J_1 & J_2 \cdots & J_i \cdots & J_n \end{bmatrix}^{\mathrm{T}}$$

$$\mathbf{K}(\in \mathbb{R}^{m \times 1}) = \begin{bmatrix} K_1 & K_2 \cdots & K_k \cdots & K_m \end{bmatrix}^{\mathrm{T}}$$

$$\mathbf{B}(\mathbf{r}_s) = \begin{bmatrix} B_{sr} & B_{ss} \end{bmatrix}^{\mathrm{T}}$$

For a given EM/conductor configuration, **J**, **K** and **B**( $\mathbf{r}_s$ ) can be derived in state-space representation using (5), (4) and (6) with the MVPs and MFDs for the 2D elements calculated from (7a, b), (8a $\sim$ c) and (9a $\sim$ c):

$$\dot{\mathbf{J}} = [\boldsymbol{\alpha}] \mathbf{J} + [\boldsymbol{\beta}] \dot{u} \tag{10a}$$

$$\mathbf{K} = [\mathbf{a}]\mathbf{J} + [\mathbf{b}]u \text{ and } \mathbf{B}(\mathbf{r}_s) = [\mathbf{C}]\mathbf{J} + [\mathbf{D}]\mathbf{K}$$
 (10b,c)

The system and input matrices in (10a) can be solved as

$$[\boldsymbol{\alpha}] = -\frac{1}{\sigma \mu_{\star}} ([\mathbf{F}_{\nu}] + \gamma [\mathbf{F}_{b}] [\mathbf{L}] [\mathbf{G}_{\nu}])^{-1}$$
 (11a)

$$[\boldsymbol{\beta}] = \sigma[\boldsymbol{\alpha}] (\mathbf{u}_f + \gamma [\mathbf{F}_b] [\mathbf{L}] \mathbf{u}_g)$$
 (11b)

where 
$$[\mathbf{L}] = [\mathbf{I}_m] - \gamma [\mathbf{G}_b]$$
; and (11c)

 $[\mathbf{I}_m]$  is a  $m \times m$  identity matrix.

The elements of  $\mathbf{F}_{\nu}(\in \mathbb{R}^{n \times n})$ ,  $\mathbf{F}_{b}(\in \mathbb{R}^{n \times m})$ ,  $\mathbf{G}_{\nu}(\in \mathbb{R}^{m \times n})$  and  $\mathbf{G}_{b}(\in \mathbb{R}^{m \times m})$  in 11(a, c) can be computed from (8c) and (9c),

and are given by  $\hat{v}_l f_{il}^v$ ,  $\hat{s}_k f_{ik}^b$ ,  $\hat{v}_l g_{kl}^v$  and  $\hat{s}_i g_{kl}^b$  respectively, where the double-subscripts "mn" in the kernels (f and g) indicate  $m^{th}$  row and  $n^{th}$  column. In (11b), the elements of  $\mathbf{u}_f (\in \mathbb{R}^{n\times 1})$  and  $\mathbf{u}_g (\in \mathbb{R}^{m\times 1})$  are given by  $f_i^e$  and  $g_k^e$  respectively. Since the MFD has two components,  $g_{ko}^*$  is determined by the surface that  $k^{th}$  element belongs:

$$g_{k_{\circ}}^{*} = \begin{cases} \pm (g_{k_{\circ}}^{*})_{r} & -z = z_{s} + d + h(1 \pm 1) / 2 \\ (g_{k_{\circ}}^{*})_{z} & r = w \end{cases}$$

Similarly, the output matrices in (10b, c) are obtained as

$$[\mathbf{a}](\in \mathbb{R}^{m \times n}) = \gamma \mu_r [\mathbf{L}]^{-1} [\mathbf{G}_v]; \tag{12a}$$

$$[\mathbf{b}](\in \mathbb{R}^{m\times 1}) = \gamma [\mathbf{L}]^{-1} \mathbf{u}_{g}; \qquad (12b)$$

$$[\mathbf{C}](\in \mathbb{R}^{2\times n}) = \mu_r \begin{bmatrix} \hat{v}_1 \mathbf{g}_{s1}^v & \hat{v}_2 \mathbf{g}_{s2}^v \cdots & \hat{v}_k \mathbf{g}_{sk}^v \cdots & \hat{v}_n \mathbf{g}_{sn}^v \end{bmatrix}; \quad (13a)$$

and 
$$[\mathbf{D}](\in \mathbb{R}^{2\times m}) = \begin{bmatrix} \hat{s}_1 \mathbf{g}_{s1}^{\nu} & \hat{s}_2 \mathbf{g}_{s2}^{\nu} & \cdots & \hat{s}_k \mathbf{g}_{sk}^{\nu} & \cdots & \hat{s}_m \mathbf{g}_{sm}^{\nu} \end{bmatrix}$$
. (13b)

The 1<sup>st</sup> and 2<sup>nd</sup> terms on the right side of the sensor output  $\mathbf{B}(\mathbf{r}_s)$  in (10c) include the contributions from the VCD and the SCD sources respectively. Since the MFD due to EM can be predetermined and subtracted from measurements, its effect is not modeled in (10c). By substituting (10b) into (10c), the sensor output  $\mathbf{B}(\mathbf{r}_s)$  can be explicitly expressed in terms of  $\mathbf{J}$  and u as shown in (14a) where  $\mathbf{B}_{\sigma}$  depends on both the electrical conductivity and the permeability of the conductor but  $\mathbf{B}_{\mu}$  is simply influenced by the permeability and equivalent to  $\mathbf{B}(\mathbf{r}_s)$  in a static magnetic field:

$$\mathbf{B}(\mathbf{r}_{s}) = \mathbf{B}_{\sigma}(\mathbf{r}_{s}) + \mathbf{B}_{\mu}(\mathbf{r}_{s}) \tag{14a}$$

where 
$$\mathbf{B}_{\sigma}(\mathbf{r}_{s}) = \mu_{r}([\mathbf{C}] + \gamma[\mathbf{D}][\mathbf{L}]^{-1}[\mathbf{G}_{v}])\mathbf{J}$$
 (14b)

and 
$$\mathbf{B}_{\mu}(\mathbf{r}_s) = (\gamma^2 [\mathbf{D}] [\mathbf{F}_b]^{-1} \mathbf{u}_g u$$
. (14c)

#### **RESULTS AND DISCUSSION**

The objectives and results are organized as follows:

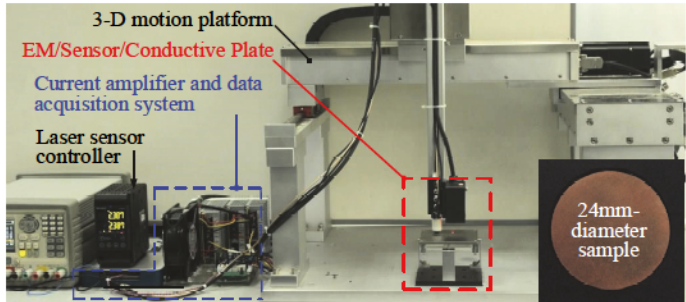
- The DCS method for modeling both nonmagnetic and weakly magnetized samples were validated experimentally. The effects of the magnetic permeability on the measured MFDs are examined by comparing results simulated with and without magnetic properties.
- With the validated DCS model, an investigation was conducted numerically to verify its accuracy by comparing simulated results against FEA computed using a popular commercial software (COMSOL Multiphysics) to provide a basis for comparison; both harmonic and pulsed EM excitations are considered.
- The effectiveness of the DCS models was numerically evaluated for simultaneous measurements of the geometrical (distance and thickness) and material (permeability and conductivity) properties.

## Experimental validation

The experimental setup is shown in Fig. 2 where an EC-sensor described in [12] is positioned by a 3D precision translation stage to control its distance d from the test sample. Two annular conductive samples (nonmagnetic copper and bronze alloy that has a weak magnetic permeability) were used in the experiment; their detailed parametric values are listed in Table I. Sinusoidal currents (with frequency from 100 Hz to 25k Hz) were used in the experiments. Since  $\dot{\bf j} = j\omega {\bf J}$  and  $u = (j\omega)u$ , (10a) reduces to

$$\mathbf{J} = j\omega (j\omega [\mathbf{I}_n] - [\boldsymbol{\alpha}])^{-1} [\boldsymbol{\beta}] u \tag{15}$$

The z-direction MFDs generated by the induced eddy-current and the magnetization effects are measured, from which the magnitudes and phases can be extracted. The MFD measurements (with d=2, 3, 4, 5mm) are compared with the DCS-based simulations for the <u>nonmagnetic</u> ( $\mu_r=1$ ) copper and the <u>weakly magnetized</u> ( $\mu_r=1.15$ ) bronze-alloy samples in Figs. 3 and 4 respectively, which show excellent agreements.



(a) Experimental testbed

(b) Test sample

FIGURE 2. EXPERIMENTAL SETUP.

TABLE I. PARAMETERS OF EC-SENSOR AND SAMPLES

EC-sensor		Samples	Copper	Bronze
$(a_o, a_i, a) \text{ mm}$	(6,3.75,2)	(w, h) mm	(12, 5.38)	(12,5.5)
$(r_s, z_s)$ mm	(6, 4.5)	$\sigma$ MS/m	58.4	5.27
Coil	60 turns	$\mu_r$	1	1.15
Distance d (mm)		2, 3, 4, 5		
Frequency range (Hz)		100 to 25k		

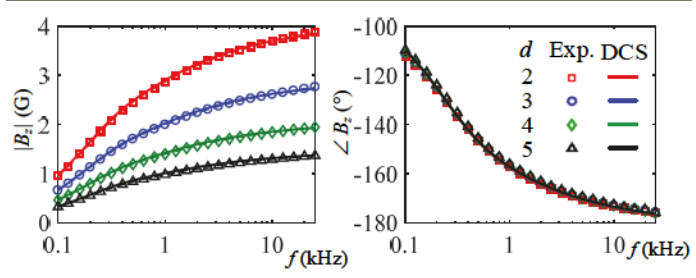


FIGURE 3. MEASURED MFD RESPONSES OF EDDY-CURRENT INDUCED IN COPPER,  $\mu_r$ = 1.

Figure 4 illustrates the effects of the magnetic permeability on the measured MFDs by comparing simulated results with  $\mu_r$ = 1 (nonmagnetic) and  $\mu_r$ =1.15 for the weakly magnetized bronze alloy sample. As in Fig. 3,  $\angle B_z$  is independent of the distance d for a specified conductor thickness h. The comparisons show that the magnetic permeability has an effect

on the measured MFD especially at low frequencies. For nonmagnetic materials,  $|B_z|$  and  $\angle B_z$  approach 0 and  $-90^\circ$  respectively as the frequency decreases. In contrast,  $|B_z|$  approaches a non-zero constant  $B_\mu$  as derived in (14b) for a magnetic material. Since  $B_\mu$  is proportional to the input current and has only a real part,  $\angle B_z$  approaches zero instead of  $90^\circ$ .

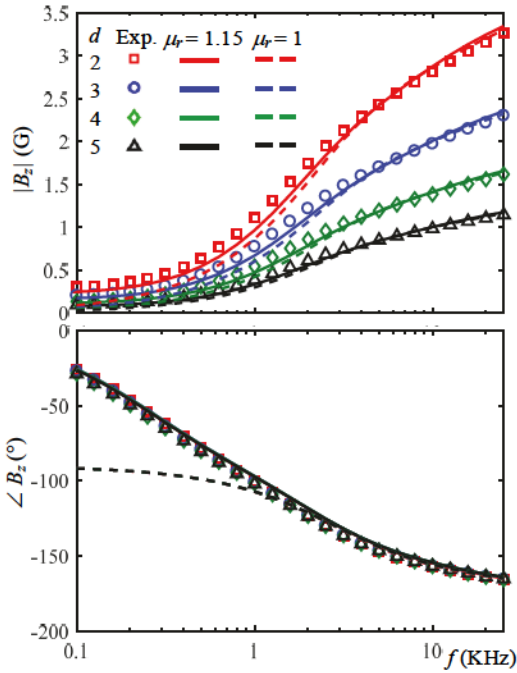


FIGURE 4. MEASURED MFD RESPONSES OF INDUCED EDDY-CURRENT MAGNETIZATION OF THE BRONZE-ALLOY,  $\mu_{r}$ = 1.15.

## Numerical investigation using harmonic excitation

The accuracy of the DCS models is numerically verified by comparing computed results of the eddy current J (0.25mm below the conductor surface), the equivalent surface current K (top surface) and the MFD (measured at d=1mm) with that simulated using a 2D axis-symmetric COMSOL model with triangular elements (minimum size of 0.5mm). Since COMSOL cannot directly obtain the surface current, the results were computed from the magnetization vector defined in (1b). The conductor in DCS model was divided into uniform volumes and surface elements (0.5mm size). The number of elements/meshes used in DCS model and COMSOL for a 2mm thick conductor are listed in Table II. COMSOL requires to model a sufficiently large air space, and thus a much larger number of elements than the DCS method.

TABLE II. SIMULATION PARAMETERS FOR HARMONIC EXCITATION

WINDER IN SHITTER THE PROPERTY OF THE EXCHANGES					
Harmonic Validation		Skin-effect Analysis			
(w, h), d mm	(20, 2), 1	Thickness h, mm	1, 2, 3, 4		
$\sigma, \mu_r$	10 MS/m, 10	Range of skin-depth $\delta$ (mm)	0.1-10		
$f = \omega/2\pi$	100 Hz				
DCS	160 volume elements; 84 surface elements				
COMSOL	1276 volume elements				

Using the same EC-sensor (Table I) excited with a 100Hz

sinusoidal current) and parametric values listed in Table II, the simulation results are summarized in Figures 5 and 6.

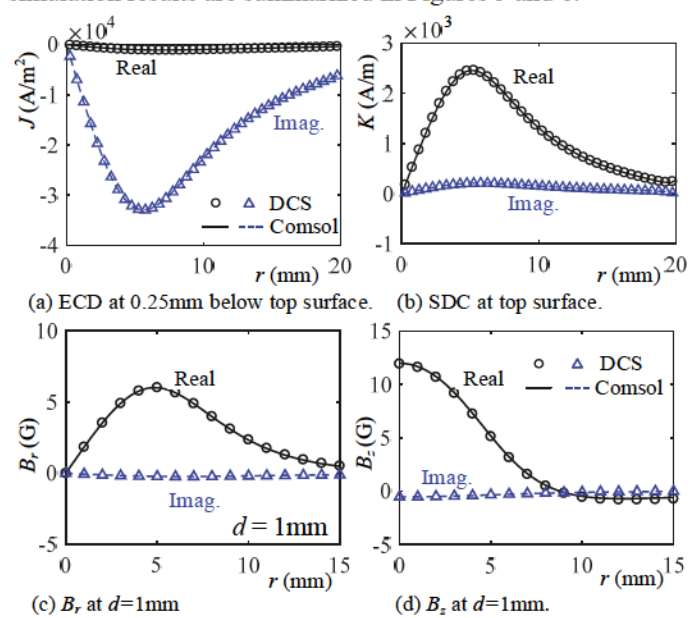


FIGURE 5. SIMULATION HARMONIC RESPONSES.

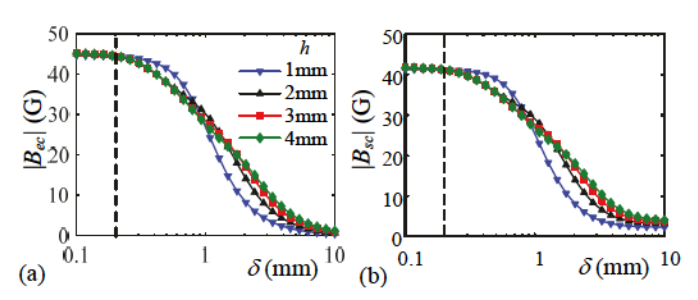


FIGURE 6. SKIN-DEPTH EFFECTS ON CONDUCTOR GENERATED MFD

The following are observations drawn from the results:

- As compared in Figure 5(a, b), both the ECD and SCD plots calculated from the DCS model are identical to that simulated in COMSOL. The MFD (generated by the EC and the magnetization effect) was further compared with the COMSOL results in Figures 5(c, d). The agreements (between DCS-computed and FEA simulated MFDs) verify the accuracy of the DCS models.
- As shown in Figures 5(a, b), the ECD is mainly contributed by its imaginary part. In contrast, the SCD is contributed by its real part. Figures 5(c, d) show that the imaginary parts of both  $B_r$  and  $B_z$  are very small as compared to the real parts, implying that the conductor-generated MFD is mainly generated by the magnetization effects.
- Figures 6(a, b) where  $\delta = \sqrt{2/(\omega \mu_0 \mu_r \sigma)}$  is the EC skin depth simulate the "measured  $B_z$ " contributed by the EC (volume) and by the surface-current for four different h values (1, 2, 3 and 4mm), which are denoted by  $B_{ec}$  and  $B_{sc}$ , respectively. As shown in Figures 6(a, b), the MFDs caused by the EC and SC show similar trends; both increases

as  $\delta$  decreases. When  $\delta \ll h$ ,  $B_z$  is insensitive to the conductor thickness h for both magnetic and nonmagnetic materials.

The only difference (between B<sub>ec</sub> and B<sub>sc</sub>) is that as Sh increases, B<sub>ec</sub>→0 whereas B<sub>sc</sub> approaches a non-zero constant corresponding to the measured MFD for an EM subjected to a constant excitation.

## Numerical investigation using pulse excitation

The system response to a non-harmonic input can be analyzed in time domain by discretizing the state equation (10a) using Euler approximation, which leads to (16) where  $\Delta T$  is the sampling period:

$$\mathbf{J}(k+1) = ([\mathbf{I}_n] + \Delta T[\boldsymbol{\alpha}])\mathbf{J}(k) + \Delta T[\boldsymbol{\beta}]u(k)$$
 (16)

With known initial conditions, (16) can be solved iteratively for the ECD for a specified input. A rectangular pulse excitation commonly used in geometrical and material measurements is described here as an illustrative non-harmonic example:

$$u(t) = \begin{cases} 1 & t \le t_0 \\ \exp[(t - t_0) / \tau] & t > t_0 \end{cases}$$
 (17)

In (17),  $t_0$  is a time-delay period for estimating the magnetic permeability  $\mu_t$ ; and  $\tau$  is the time constant to account for the coil inductance in the circuit. The following discussions assume that only  $B=B_z$  is measured. The results are organized in three subsections:

- 1) Model validation for non-harmonic excitaion.
- 2) Estimation of material properties  $(\mu_r, \sigma)$ .
- 3) Estimation of geometrical properties (d, h).

The parametric values used in the numerical investigations are summarized in Table III.

TABLE III. SIMULATION PARAMETERS FOR PULSE EXCITATION

	$(\mu_r, \sigma)$ estimation	(d,h) estimation		
(d, h) mm σ, MS/m	(1, 2)	(1 to 4, 1 to 4)		
$\sigma$ , MS/m	2, 4, 6, 8, 10	10		
$\mu_r$	1 to 200	10		
$(t_0, \tau) = (0.1, 0.01) \text{ ms}; \Delta T = 0.001 \text{ms}.$				

Model validation for non-harmonic excitation

Using (11a, b) with  $\Delta T=1$  microsecond, Figure 7(a) graphs the simulated transient response of the measured  $B_z$  for both magnetic ( $\mu_r = 10$ ) and nonmagnetic ( $\mu_r = 1$ ) conductors.

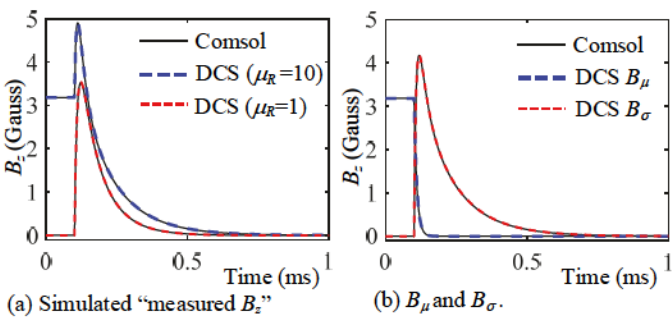


FIGURE 7. SIMULATION RESULTS FOR TRANSIENT EXCITATION

To gain physical insights to the measured MFD for

estimating the magnetic permeability  $\mu_r$ , the MFD measurement is divided into two parts in (14a). For a sensor-conductor configuration, the kernel functions defined in (8a~c) and (9a~c) are known constants. Thus,  $B_\mu$  is proportional to the excitation current with a proportional factor that can be determined from the measured MFD at t=0; and  $B_\sigma$  can be obtained by subtracting  $B_\mu$  from the measurements. Mathematically,  $B_\mu$  and  $B_\sigma$  can be written as:

$$\frac{B_{\mu}(t)}{B_0} = \frac{u(t)}{u_0}; \frac{B_{\sigma}(t)}{B_0} = \frac{B(t)}{B_0} - \frac{u(t)}{u_0}$$
 (18a, b)

In (18a) and (18b),  $B_{\theta}$  and  $u_{\theta}$  are the measured MFD and current respectively (at t=0). The computed  $B_{\mu}$  and  $B_{\sigma}$  are plotted in Figure 7(b), revealing the fact that the shape of the  $B_{\sigma}$  curve is similar to that of the measured MFD assuming the conductor is nonmagnetic but with a different peak value. This finding suggests that  $B_{\sigma}$  is also influenced by  $\mu_r$ .

As compared with COMSOL simulations, all plots in Fig. 7(a, b) agree well with the FEA, demonstrating the DCS models can be used to calculate the *J*, *K* and **B** fields for any arbitrary excitation. The calculation time of DCS method and COMSOL is also compared when running on a PC Platform (Intel Core *i*7-2600 CPU @3.40GHz, 15GB RAM, 640bit OS). The DCS method needs 47 seconds for the 1ms time domain simulation, which is only about 12% of COMSOL simulation (394 seconds), showing its great efficiency when simulating non-harmonic excitations.

Effects of material parameters  $(\mu_r, \sigma)$ 

Based on the previous analyses in  $(14a\sim c)$  and Figure. 7, the parameters  $(\mu_r$  and  $\sigma)$  can be determined from in the static magnetic field  $B_\mu$  during the time-delay period  $(t < t_0)$  and the transient response of the time-varying magnetic field  $B_\sigma$  to the step change:

<u>During the time-delay period</u>  $(t \le t_0)$ , only the magnetized MFD  $B_{\mu}$  exists when there is no induced eddy current for a magnetic conductor. Since  $B_{\mu}$  is only influenced by permeability, it can be utilized to estimate  $\mu_r$ . To best illustrate the relation of  $B_\mu$  to  $\mu_r$ ,  $\gamma$  formulated in (4b) is introduced in the discussion. As shown in Fig. 8, the left plot relates  $B_{\mu}$  to  $\gamma$  for a 2mm thick conductor under a constant excitation of 1A current, which is approximately linear. With measured  $\gamma$ , the relative permeability  $\mu_r$  can be estimated from the  $(\gamma - \mu_r)$  relationship in the right plot of Fig. 8. The relationship between  $\gamma$  and  $\mu_r$  is highly nonlinear, as  $\mu_r \rightarrow \infty$ ,  $\gamma \rightarrow 2/\mu_0$ ;  $\gamma$  reaches 90% of the asymptotic value when  $\mu_r$  increases to 19. Continuedly increasing  $\mu_r$  will cause very small change in  $\gamma$ . This finding indicates that the estimation  $\mu_r$  from the measured  $B_{\mu}$  is effective for low  $\mu_r$  materials. The measurement accuracy decreases as  $\mu_r$  increases due to the deficient definition.

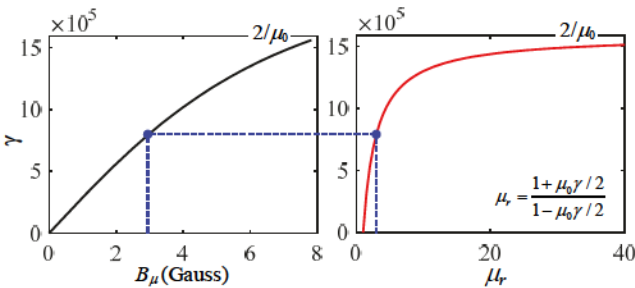


FIGURE 8. RELATIONSHIPS BETWEEN MAGNETIZED MFD AND MATERIAL PERMEABILITY

During the step response of the pulsed current excitation, both  $B_{\mu}$  and  $B_{\sigma}$  are generated. Since  $B_{\mu}$  is not related to the conductivity, it is excluded from the MFD measurement; in other words, only  $B_{\sigma}$  is considered. The  $B_{\sigma}$  responses at different  $(\sigma, \mu_r)$  combinations are simulated and compared in Figure 9(a) where the MFD responses to different specified  $(\sigma$  or  $\mu_r)$  are plotted. The peaks and time constants increase as  $\sigma$  increases; in other words, the area under the curve increases with  $\sigma$ . In contrast, the curves for the smaller  $\mu_r$  have higher peaks but decay to zero faster than those for a larger  $\mu_r$ , leading to similar areas under the curves. The findings provide a method to extract the conductivity related information by integrating the transient responses over time as in (19):

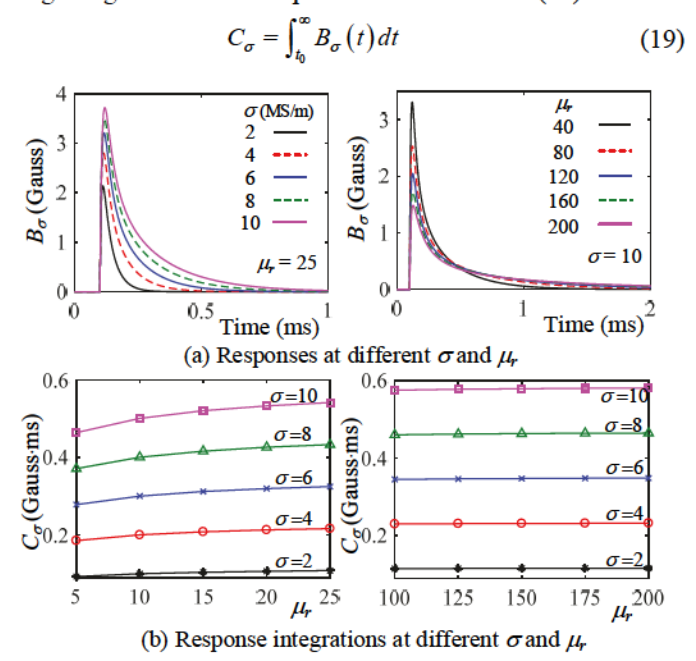


FIGURE 9. RELATIONSHIPS BETWEEN MFD RESPONSE AND MATERIAL CONDUCTIVITY

The integration values are plotted in Fig. 9(b) where two sets of permeability values are simulated. The left plots the responses of low- $\mu_r$  materials with ( $\mu_r = 5$  to 25) while the right corresponds to materials with relatively larger permeability ( $\mu_r = 100$  to 200). The left plot shows that integration values are influenced by both  $\sigma$  and  $\mu_r$  for low- $\mu_r$  material, but insensitive

to  $\mu_r$  in relative large  $\mu_r$  values. The findings indicate that the  $B_\sigma$  integral can be used to estimate the material conductivities. For materials with large  $\mu_r$ , the conductivity can be directly estimated from integration of  $B_\sigma$ , while for low- $\mu_r$  material,  $\sigma$  can be obtained with known  $\mu_r$ .

Effects of geometry parameters (d, h)

For a given material, the excitation frequency has a significant influence on very small skin-depths; the measured  $B_z$  is insensitive to the thickness h as illustrated in Figure 6; and thus can be used to determine the distance d. Once d is known, h can be found from large skin-depth measurements. The above observations provide the basis for the simultaneous (d, h) estimation for a given sensor-conductor configuration.

Since the rectangle pulse current (17) contains an infinite number of frequency components, from which high and low frequency components can be extracted by means of a high-pass and a low pass filters respectively. The filtered results can be individually integrated over time leading to a pair of high and low frequency indices  $C_h$  and  $C_l$ :

$$C_h = \int_{t_0}^{\infty} \left| B_h(t) \right| dt; C_l = \int_{t_0}^{\infty} \left| B_l(t) \right| dt$$
 (20a, b)

To illustrate the method for simultaneous (d, h) estimation using a single pulse current estimation, the filtered  $(B_l, B_h)$  and the integrated  $(C_l, C_h)$  are simulated with the (low, high) pass cut-off frequencies (100Hz, 15kHz) which correspond to a (4mm, 0.4mm) skin depth in Figures 10(a, b) and 10(c, d) respectively. From  $C_h$ , the distance can be first measured. Once d is known, the thickness h can be estimated from  $C_l$ .

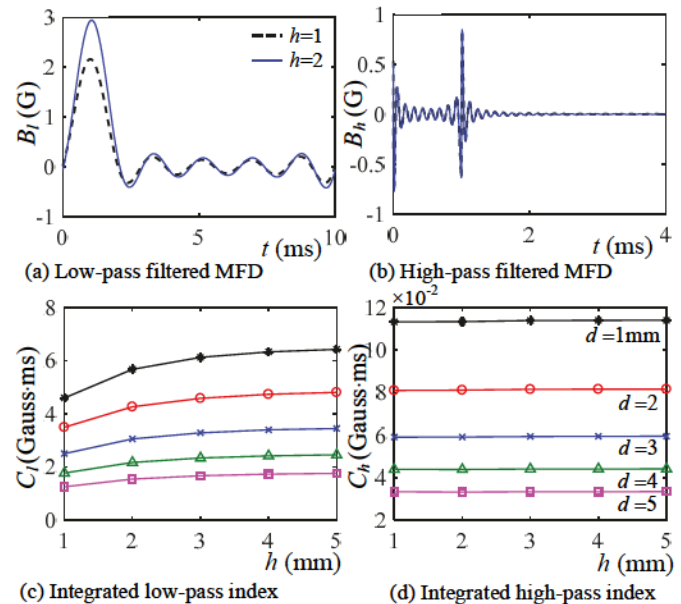


FIGURE 10. SIMULTANEOUS ESTIMATION OF DISTANCE AND THICKNESS USING A SINGLE PULSED-CURRENT EXCITATION.

#### CONCLUSION

A state-space model for analyzing the dynamic response of eddy current in magnetic conductors has been derived. The DCS model offers closed-form solutions to the ECD field, the equivalent surface-current due to the magnetization and its corresponding generated MFD. The model was experimentally validated and further verified with FEA results, the comparisons between the DCS and the benchmark FEA solutions show excellent agreements and much less computing time (12% of COMSOL for time-domain simulation), demonstrating the model accuracy and its effectiveness for both harmonic and pulsed inputs. The feasibility of the DCS models for multi-parameter (geometrical and material parameter) measurements using combined high and low frequency excitation has been numerically investigated. The results illustrate that the high-frequency components of measured MFD are thickness insensitive. When combined with lowfrequency measurements, the distance and thickness information can be measured simultaneously. The results further suggest that the MFD responses under static magnetic field are only dependent on permeability, whereas the pulse transient MFD response can be used to estimate conductivity; these findings provide essential bases for material property measurements.

#### REFERENCES

- [1] Lee, Kok-Meng, Hao, Bingjie, Li, Min and Bai, Kun. "Multi-parameter eddy-current sensor design for conductivity estimation and simultaneous distance and thickness measurements." *IEEE Transsactions on Industrial Informatics* (2018): DOI: 10.1109/TII.2018.2843319.
- [2] Chen, Xingle and Lei, Yinzhao. "Electrical conductivity measurement of ferromagnetic metallic materials using pulsed eddy current method." NDT & E International Vol. 75 (2015): pp. 33-38.
- [3] Bae, Jae-Sung, Moon, K. Kwak, and Daniel, J. Inman. "Vibration suppression of a cantilever beam using eddy current damper." *Journal of Sound and Vibration* Vol. 284 (2005) No. 3-5 pp. 805– 824
- [4] Chen, Shia-Chung, Jong, Wen-Ren and Chang, Jen An. "Dynamic mold surface temperature control using induction heating and its effects on the surface appearance of weld line." *Journal of Applied Polymer Science* Vol. 101 No. 2 (2006): pp.1174-1180.
- [5] De Geeter, Nele, Guillaume, Crevecoeur and Luc Dupré. "Eddy-current simulations using an independent impedance

- method in anisotropic biological tissues." *IEEE Trans. on Magnetics* Vol. 47 No. 10 (2011): pp. 3845-3848.
- [6] Dodd, C. V., and W. E. Deeds. "Analytical solutions to eddycurrent probe-coil problems." J. Appl. Phys. Vol. 39 No. 6 (1968): pp. 2829–2838.
- [7] Theodoulidis, Theodoros and Epameinondas, Kriezis. "Series expansions in eddy current nondestructive evaluation models." J. of Materials Processing Technology Vol. 161 No. 1-2 (2005): pp. 343-347.
- [8] Fava, Javier O. and Marta, C. Ruch. "Calculation and simulation of impedance diagrams of planar rectangular spiral coils for eddy current testing." NDT & E International. Vol. 39 No. 5 (2006): pp. 414–424.
- [9] Yu, Yating, Yan, Yue, Wang, Fei, Tian, GuiYun and Zhang, Dejun. "An approach to reduce lift-off noise in pulsed eddy current nondestructive technology." NDT & E International Vol. 63 (2014): pp. 1-6.
- [10] Gao, Yunlai, Tian, GuiYun, Li, Kongjing, Ji, Juan, Wang, Ping and Wang, Haitao. "Multiple cracks detection and visualization using magnetic flux leakage and eddy current pulsed thermography." Sensors and Actuators A: Physical Vol. 234 (2005): pp. 269-281.
- [11] N. Ida and J. P. A. Bastos. "Forces in permanent magnets team workshop problem 23." (2006). [Online]. Available: http://www.compumag.org/jsite/images/stories/TEAM/problem2 3.pdf
- [12] Lin, Chun-Yeon, Lee, Kok-Meng and Hao, Bingjie. "Distributed current source method for modeling magnetic and eddy-current fields induced in non-ferrous metallic objects." *IEEE/ASME Transactions on Mechatronics* (2017): DOI: 10.1109/TMECH.2017.2771763.
- [13] Malekipour, Ehsan and Hazim, El-Mounayri, "Common defects and contributing parameters in powder bed fusion AM process and their classification for online monitoring and control: a review." The International Journal of Advanced Manufacturing Technology Vol. 95 No. 1-4 (2017): pp. 527-550.
- [14] Wang, Zhuqing, Todd A. Palmer and Allison M. Beese. "Effect of processing parameters on microstructure and tensile properties of austenitic stainless steel 304L made by directed energy deposition additive manufacturing." Acta Materialia Vol. 110 (2016): pp. 226-235.
- [15] Lim, Jungyoul and Lee, Kok-Meng. "Distributed multilevel current models for design analysis of electromagnetic actuators." *IEEE/ASME Trans. on Mechatronics* Vol. 20 No. 5 (2015): pp 2413-2424.